KAPL-P-000174
(K97058)

CONF-9705119--

GaInSb and GaInAsSb THERMOPHOTOVOLTAIC DEVICE FABRICATION AND CHARACTERIZATION

G. Charache, C. Hitchcock, et. al.

May 1997

NOTICE

KAPL ATOMIC POWER LABORATORY SCHENECTADY, NEW YORK 10701

Operated for the U. S. Department of Energy
by KAPL, Inc. a Lockheed Martin company

DISCLAIMER

GaInSb and GaInAsSb Thermophotovoltaic Device Fabrication and Characterization

C. Hitchcock, R. Gutmann, J. Borrego, H. Ehsani, and I. Bhat
Center for Integrated Electronics and Electronics Manufacturing
Department of Electrical, Computer, and Systems Engineering
Rensselaer Polytechnic Institute, Troy, New York 12180
and
M. Freeman and G. Charache
Lockheed Martin, Inc., Schenectady, New York 12301

Abstract

Thermophotovoltaic (TPV) devices have been fabricated using epitaxial ternary and quaternary layers grown on GaSb substrates. The GaInSb layers were grown by organometallic vapor phase epitaxy (OMVPE) and the InGaAsSb lattice-matched layers were grown by liquid phase epitaxy (LPE). Device fabrication steps include unannealled p-type ohmic contacts, annealed Sn/Au n-type ohmic contacts, and a thick Ag top-surface contact using a lift-off process. Devices are characterized primarily by dark I-V, photo I-V, and quantum efficiency measurements, which are correlated to microscopic and macroscopic material properties. Particular emphasis has been on material enhancements to increase quantum efficiency and decrease dark saturation current density. TPV device performance is presently limited by the base diffusion length, typically 1 to 2 microns.

1 Introduction

This paper presents the fabrication and characterization of ternary (GaInSb) and quaternary (GaInAsSb) device layers grown on GaSb substrates, extending earlier results [1]. For current devices, all active layers have bandgaps in the 0.52eV to 0.56eV range. The lattice constants of the ternary structures are, of necessity, not matched to that of the binary (GaSb). However, the added complexity of the fourth element (As) in quaternaries allows matching the lattice constant of the epilayers to the substrate while varying the bandgap. The epitaxial growth conditions and characterization of the epitaxial material are presented elsewhere [2]. Here the fabrication and characterization of thermophotovoltaic devices using the epitaxial layers as starting material are presented.

2 Epitaxial Structures and Junction Processing

Both ternary (GaInSb) and quarternary (GaInAsSb) epitaxial layers grown on GaSb substrates have been used in fabricating and characterizing p-n junctions for TPV applications. The ternary device structures were produced by OMVPE, with the quaternary device structures produced by LPE. The junctions that have been fabricated and characterized are grouped into three "generations," corresponding to the general time frame of fabrication.

Technology	Generation 1	Generation 2	Generation 3
Ternary OMVPE	X	X	X
Quaternary LPE	X	X	

Table 1: Device Fabrication and Characterization

An overview of fabrication and characterization to date is shown in table 1, where the 'X' indicates one or more device process lots to be presented. Most complete results have been obtained with generation 1 and 2 devices.

The ternary device structures are shown in figure 1. These generation 1 and generation 2 structures were initial structures with parameters chosen primarily based upon preliminary material studies and first-order device design. The generation 3 structure, however, contains layers with variable thicknesses and dopings in order to study the effects of individual parameter variations on device performance. In all three cases, the grown epi-layers were not lattice matched to the underlying GaSb. A series of graded layers varying from $Ga_{1.0}In_{0.0}Sb$ at the substrate to the approximately $Ga_{0.8}In_{0.2}Sb$ of the device region, separate the substrate from the base region.

The quaternary device structures shown in figure 2 were fabricated by LPE. Generation 1 and 2 were identical except that generation 1 relied upon parasitic gallium anti-site defects for emitter doping, while the generation 2 emitter was doped with germanium. For both structures, the quaternary epi-layers were approximately $Ga_{0.8}In_{0.2}As_{0.2}Sb_{0.8}$, producing the desired bandgap and a lattice match to the GaSb substrate.

At the start of the fabrication process, the samples were prepared by cleaning in solvents. Successive immersions in trichloroethane, acetone, methanol, and isopropanol followed by an immersion in concentrated sulfuric acid were used to remove organic contaminants. An immersion in a solution of dilute hydrochloric acid and sodium potassium tartrate removed native oxide [3].

A blanket n-type contact was then applied to the sample back surface by e-beam evaporation. Next the p-type front contact was formed by e-beam deposition and liftoff. The liftoff photolithography process for thick grid lines necessary for low series resistance is described in appendix Appendix A.

Contact metals were chosen in order to provide good ohmic contacts and good adhesion to the semiconductor substrates. For gallium antimonide and related compounds containing up to 20% indium and arsenic, the Fermi level is pinned near the valence band of the semiconductor, regardless of the work function of the contact metal [4]. As a result, contacts to p-type materials are generally ohmic as deposited, while those to n-type material must be alloyed.

For p-type contacts, 2000Å of an alloy of gold with 8% zinc, popular for gallium arsenide p-type contacts, was initially used [5]. In preliminary studies, these contacts were deposited

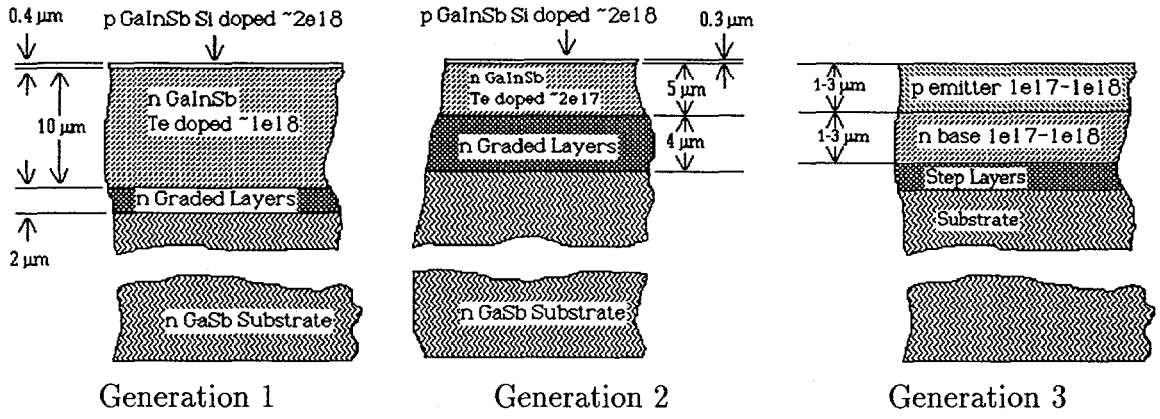

Figure 1: Ternary Structures

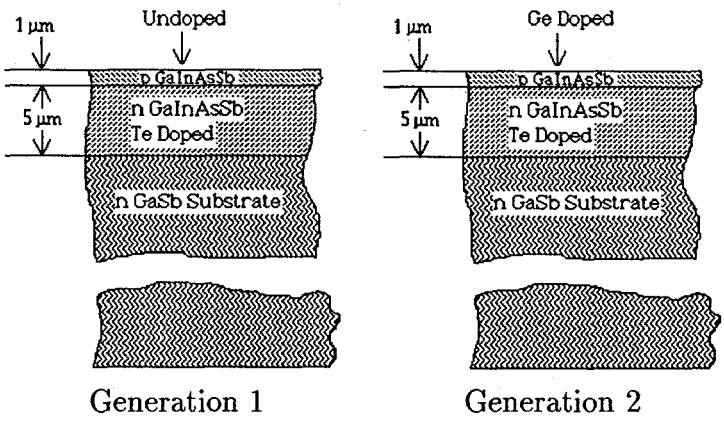

Figure 2: Quaternary Structures

1. Sample Cleaning and Oxide Removal
2. Back Contact Deposition and Anneal
3. Front Contact Deposition
4. Mesa Etch

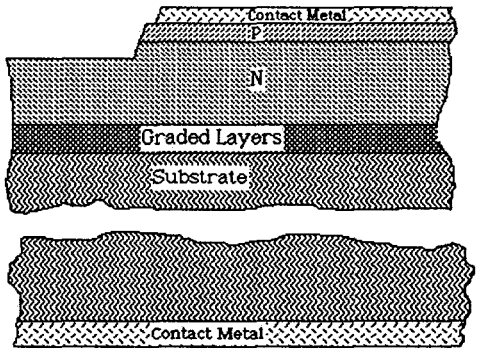

Figure 3: Baseline Device Processing and Finished Device Structure

on bulk GaSb, alloyed at 350°C for 5 seconds, and measured using the method of Cox and Strack [6][7]. The measured specific contact resistances were on the order of 10^{-5} Ωcm^2. Actual values of the contact resistance were uncertain, as the measurements were taken near the detection limit of the apparatus. Device contacts were capped with 1 to 2 microns of silver to provide a good surface for probing and to ensure that the contact metal was an equipotential surface.

During device fabrication, we found that alloyed gold-based ohmic contacts to thin p-type emitters were found to short the emitter to the base. Since nonalloyed ohmic contacts appeared to produce adequately low specific contact resistances, the fabrication procedure was changed to avoid alloying the front contact. For some devices, the metallization was changed to 300Å of titanium capped with 1 to 2 microns of silver.

For n-type contacts, an evaporation of 100Å tin followed by 2000Å of gold was employed [8]. In this case, the unalloyed contact was definitely non-ohmic, and an anneal was required. Like the gold-based p-type contact, the gold-based n-type contact shorted the device emitter to the base when alloyed on a thin emitter of these n-on-p devices. Because of the lack of shallow n-type ohmic contacts, all of the devices described have p-emitters. The n-type backside device contacts of these p-on-n devices were capped with 1 to 2 microns of silver.

After the front contact deposition, individual devices on the samples were isolated by etching the device layers in the non-active areas. A hydrochloric acid, sodium potassium tartrate, and hydrogen peroxide solution was used [9], with photoresist protecting the optically sensitive areas of the devices. In some cases, the contacts were also protected, while in others the contacts were left exposed to self align the mesas to the edges of the contacts and reduce the uncertainty in the optical areas of the devices.

3 Junction Characterization Techniques

In order to determine the underlying physics of the semiconductor junctions, the current flowing through each junction was measured as a function of voltage applied across the device to obtain the junction I-V characteristics. A curve tracing instrument (oscilloscope and associated drive electronics) was used to measure junction behavior qualitatively, while a microcomputer with an analog-to-digital/ digital-to-analog adapter was used to take more quantitative measurements.

Due to the high current, low voltage nature of thermophotovoltaic devices, Kelvin contacting methods were used for both front and rear contacts. Contact was made to the front of the device using both a current and a voltage microprobe. Contact to the rear of the device was achieved using a metal clad insulating board which had been patterned to produce independent voltage and current contacts to the device backside metallization. The deposition of a thick layer of metal on both front and rear device contacts during processing was critical to the assumption that the metal contacts could be considered as equipotential surfaces, a necessary condition for Kelvin contacting.

Room temperature dark I-V measurements were taken in both the forward and reverse directions using the apparatus described above. Comparison was made between the experimental results and theoretical models for expected device behavior using the following

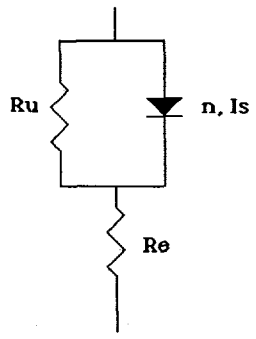

Figure 4: Circuit Model for Dark I-V Measurements

relationship:

$$I = I_s \cdot \left[exp\left(\frac{q(V - I \cdot R_e)}{nkT} \right) - 1 \right] + \frac{V - I \cdot R_e}{R_u} \tag{1}$$

where I represents device current, I_s represents saturation current, V represents the applied voltage, n is an ideality factor that should according to theory range between 1 and 2 for various regions of device operation, R_e is the series resistance, R_u is the shunt resistance, and kT is the thermal energy. This equation fit the room temperature I-V data quite well in most cases. The circuit diagram corresponding to equation (1) is shown in figure 4.

In addition to measuring I-V curves at room temperature, dark I-V curves were also measured at temperatures down to 10K. Observing the temperature dependences of the ideality factor, saturation current, and the resistances can be used to determine their physical origins. These measurements were less conclusive, but clearly can be used to assist in delineating fundamental transport mechanisms.

In addition to measuring I-V characteristics of non-illuminated devices, optically sensitive devices were also measured under high illumination conditions. This measurement is of importance not only because the test device is under conditions close to the working environment of a device in a TPV power generation system, but also because these measurements provide information about the physical origins of junction parameters. In the simplest case of a TPV device described accurately by the model of equation (1) with $R_e = 0$ and R_u infinite, the modification is to put a current source corresponding to carrier generation in series with the entire device, leading to the device model:

$$I = I_s \cdot \left[exp\left(\frac{qV}{nkT} \right) - 1 \right] - I_L \tag{2}$$

where I_L is the magnitude of the light generation current. For the more intricate model with parasitic resistances, the problem is complicated by the fact that some of the circuit elements will be in series with the generation current source, while others will be in parallel. Establishing a circuit model which fits the data will determine which of the circuit elements are associated with the device junction itself and which are associated with parasitic elements.

Several possibilities for simple circuit models are shown in figure 5. The first model is the simplest, formed from the dark model by putting a current source in series with some of

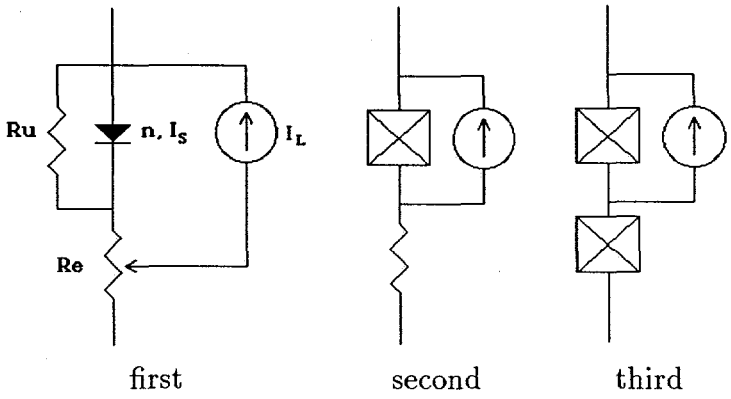

Figure 5: Light I-V Device Models

the circuit elements. A second, more general model replaces the bypassed circuit elements by a general passive two terminal device. The transfer function of the unknown device can be determined by measuring the dark I-V characteristic of the device. The third model allows for nonlinear circuit elements not associated with the active junction by replacing the non-bypassed series resistor with a general nonlinearity. This could be necessary for non-optimized structures with parasitic rectifying junctions at the substrate-epilayer boundary, or poor ohmic contacts. These models are discussed further in Section 4.

A junction characterization technique which measures device performance under illumination is the quantum efficiency measurement. Quantum efficiency measurements differ from illuminated measurements under TPV conditions in three principal respects. First, quantum efficiency measurements occur under monochromatic illumination, with the photoresponse of the test junction measured at one particular wavelength. Second, standard quantum efficiency measurements occur at much lower levels of illumination than TPV operating conditions. Third, quantum efficiency measurements are not taken with the device biased at the maximum power point of its I-V characteristic or along a range of bias points, but only at the zero voltage (short circuit) bias point. The result of the zero bias condition is that the exponential characteristic present in the models of equations (1) and (2) evaluates to zero. The result of the lower illumination is that the voltage drop across the parasitic series resistance is insignificant. The remaining circuit model is simply the current source associated with the junction illumination:

$$I = -I_L \tag{3}$$

This current can be normalized to the illumination intensity to obtain the fraction of incident photons which produce collected electron-hole pairs as a function of wavelength. If the material absorption coefficient is know as a function of wavelength, the measured quantum efficiency can be fitted to a theoretical quantum efficiency to obtain carrier diffusion lengths in the device regions.

While the standard quantum efficiency measurement and dark current measurement provide information that can be combined to produce a theoretical operational curve for the

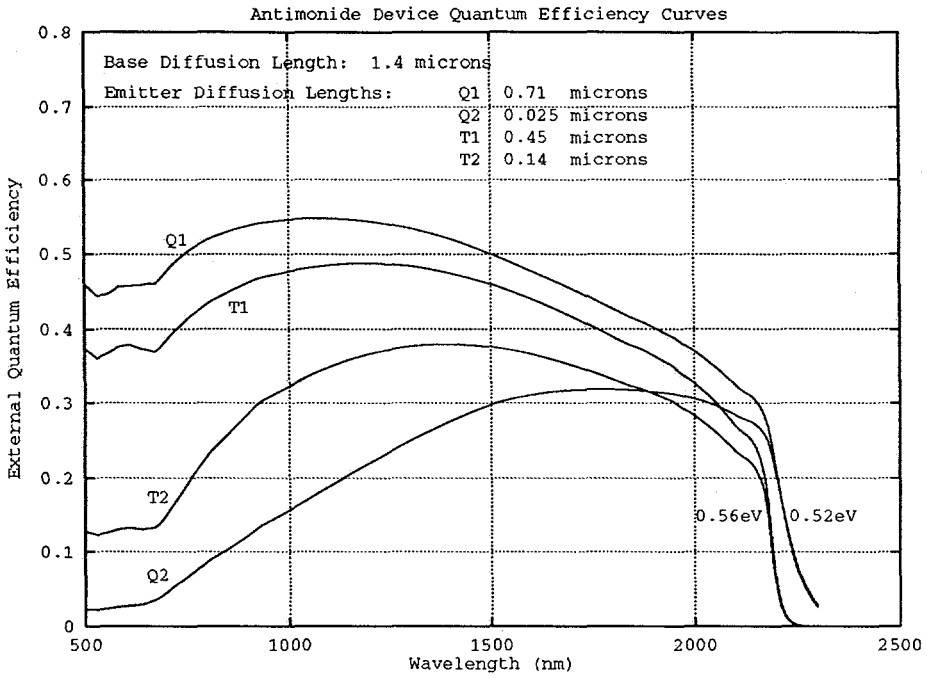

Figure 6: Fitted quantum efficiency curves for ternary (OMVPE) and quaternary (LPE) junctions, generations 1 and 2

device under any bias and illumination condition, these theoretical extrapolations depend on the linear nature of the device. A test of this assumption is to illuminate the device with a DC high intensity broad spectrum light source as well as an AC low intensity monochromatic light source and measure the AC intensity variations. If the device response to light is linear for illuminations below the high intensity DC level, the standard and high intensity quantum efficiency curves should be identical. Any variation indicates a nonlinear optical response, which can be caused by high level injection, tunneling currents, or other physical effects.

4 Junction Experimental Results and Discussion

Fitted quantum efficiency curves for the generation 1 and generation 2 devices are shown in figure 6. The curves were obtained by graphing, for each individual device, all of the experimental quantum efficiency curves on a single scale. Quantum efficiency curves were then simulated using the known parameters of the device and varying the diffusion lengths in the emitter and base to obtain the best fit. In this model a front surface recombination velocity of zero was assumed, as these thin emitter regions did not allow experimental separation of surface and bulk recombination. The base-to-substrate or base-to-graded layer surface recombination velocity was also assumed to be zero, but this approximation is not significant since the base thickness is more than 3 diffusion lengths for all generation 1 and 2 devices.

Using this approach, the emitter diffusion lengths were found to vary considerably, in

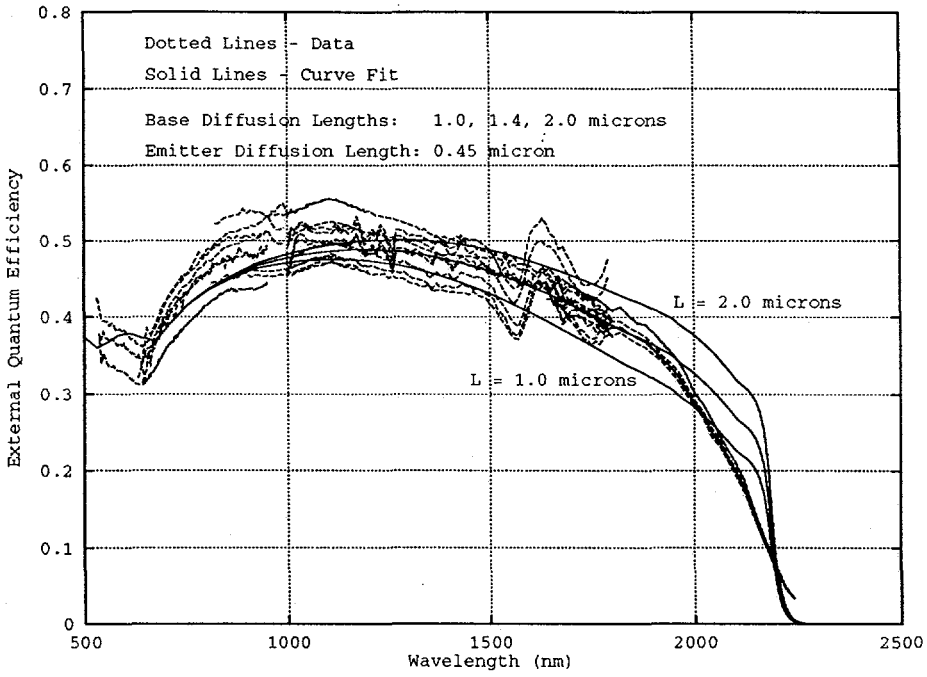

Figure 7: Quantum efficiency data and fitted curves for the generation 1 ternary device

a way that does not correlate well with any controlled or measured device parameters (see insert in figure 6). We postulate that this behavior is due primarily to effective surface recombination velocity variations at the front surface. The base diffusion lengths, however, were approximately 1.4 microns for the four devices, which is quite surprising due to the different growth techniques and process variables.

Figure 7 illustrates the curve fitting technique using the data from the generation 1 ternary device. A base diffusion length of 1.4 microns produced the best fit, while using 1.0 and 2.0 microns produced quantum efficiencies which were too low and too high, respectively. Varying the effective emitter diffusion length has a greater impact in the lower wavelength region. With such a model, the base diffusion length in the four device types shown in figure 6 was determined to be between 1.0 and 2.0 microns.

In TPV device operation, the majority of incident usable light will be in the wavelength region just below the bandgap of the device. As the absorption coefficient in this region will be lower than that in the shorter wavelength regions, the quantum efficiency in this region is determined primarily by the efficiency of the base region. Improving the 1.0 to 2.0 micron diffusion length in the base is therefore a priority in the material, processing, and device research program.

For all quantum efficiency measurements, the intensity of the monochromatic light source was approximately $50\mu W/cm^2$. In order to investigate device performance under higher intensity illumination, the monochromatic light source was supplemented, for certain measurements, with a white light source having an intensity of approximately $5mW/cm^2$. Measurements were taken by chopping the monochromatic source but not the white source, and

Technology	Generation 1	Generation 2
Ternary OMVPE	$n = 1.11$ $J_s = 0.53\ mA/cm^2$	$n = 1.30$ $J_s = 1.6\ mA/cm^2$
Quaternary LPE	$n = 1.04$ $J_s = 30\ mA/cm^2$	$n = 1.19$ $J_s = 0.98\ mA/cm^2$

Table 2: Average Fitted Parameters for Dark I-V Measurements

measuring the resulting AC response synchronously with a lock-in amplifier. The unchopped broadband illumination produced a DC response which was not measured. The curves are identical, within the range of experimental error.

The dark I-V curves of the devices under study agreed well with the device model of equation (1) and figure 4. Of the four parameters fitted by this model, the saturation current, I_s, and ideality factor, n, were reasonably consistent between measurements of nominally identical device structures; however, the series resistance, R_e, and shunt resistance, R_u, were less repeatable. Typically the series resistance varied by a factor of two but was of the order of magnitude consistent with the series resistance expected due to the $400\mu m$ substrate. The shunt resistance, however, varied by up to two orders of magnitude. A postulate that the shunt resistance is due to a small number of large area defects at the junction is compatible with the non-repeatable nature of this measurement. Summaries of the fitted parameters for the three generations of devices are shown in table 2.

Examples of low temperature (approximately 10K) dark I-V curves for generation 2 ternary devices are shown in figures 8 and 9 in comparison to room temperature data. The effective saturation current of the forward biased device decreases by almost two orders of magnitude although the reverse current decreases only by a factor of two. These relationships have not been quantified and the mechanisms for junction transport have not been delineated, particularly with the very soft reverse characteristics.

An example of a high intensity light I-V curve, taken using a photographic flash lamp to avoid heating the sample, is shown in figure 10. If this result were amenable to the analysis of either of the first two models of figure 5, it would be possible to make the light I-V curve and the dark I-V curve coincide by translation, which is not the case. This non-agreement is likely due to either parasitic nonlinearities, or a two-dimensional effect which is not accurately simulated by these one-dimensional models.

Reverse bias C-V measurements of these device junctions have, in general, not been amenable to quantitative analysis. The reverse breakdown of gallium antimonide based devices is sufficiently soft that significant reverse leakage currents obscure the results at even modest applied biases. Figure 11 shows a reverse bias C-V measurement of a generation 2 ternary device. The measurement was taken at low temperature to reduce the leakage current; however figure 9 indicates that the reverse current will remain too significant. Therefore the effect of leakage current on measured capacitance must be quantitatively determined to fully utilize C-V data as done in larger bandgap materials.

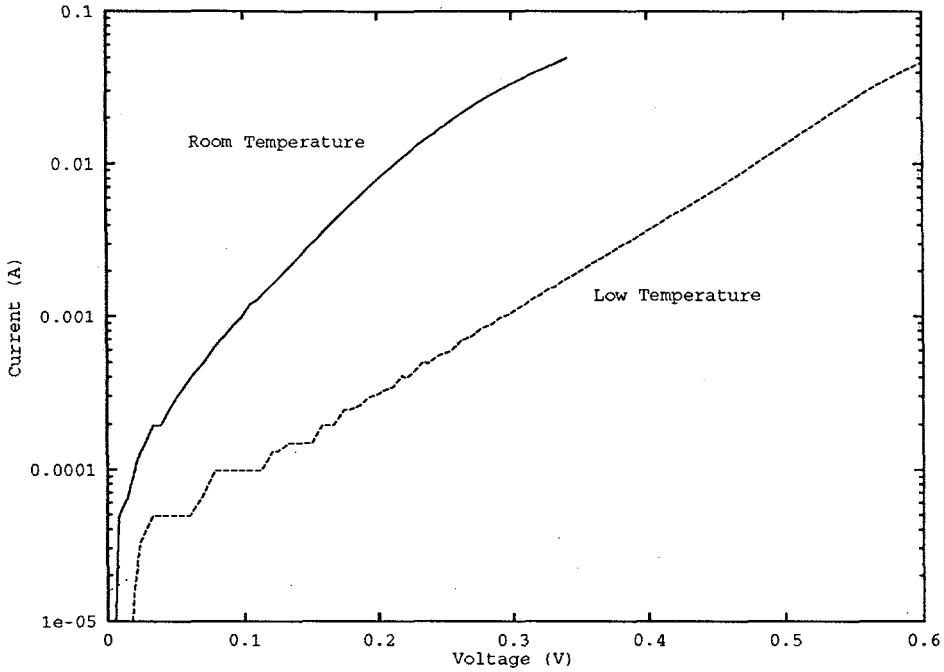

Figure 8: Low temperature (approximately 10K) forward bias dark I-V for a generation 2 ternary device

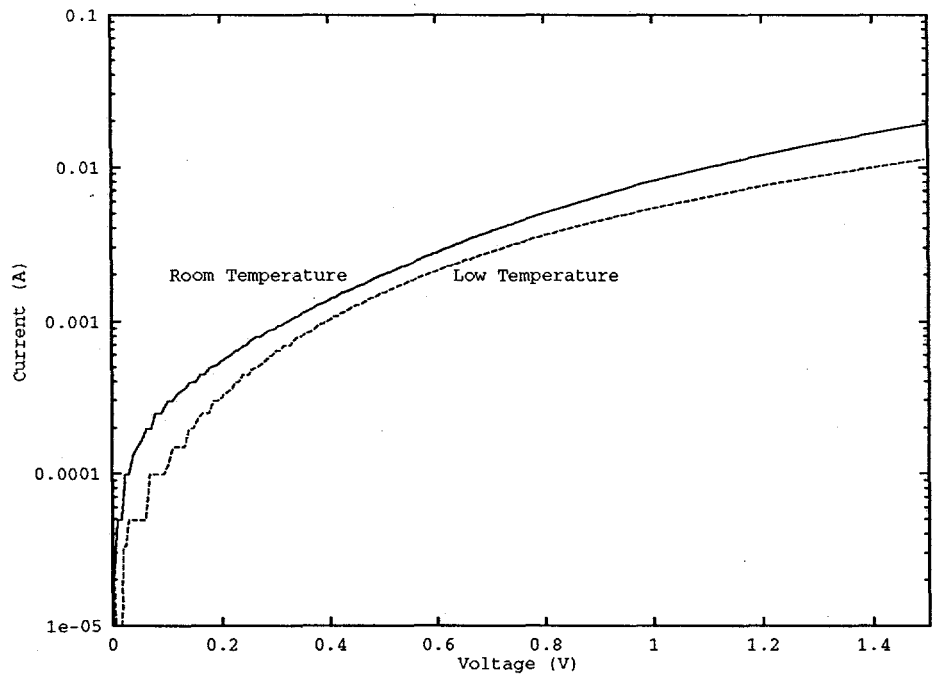

Figure 9: Low temperature (approximately 10K) reverse bias dark I-V for a generation 2 ternary device

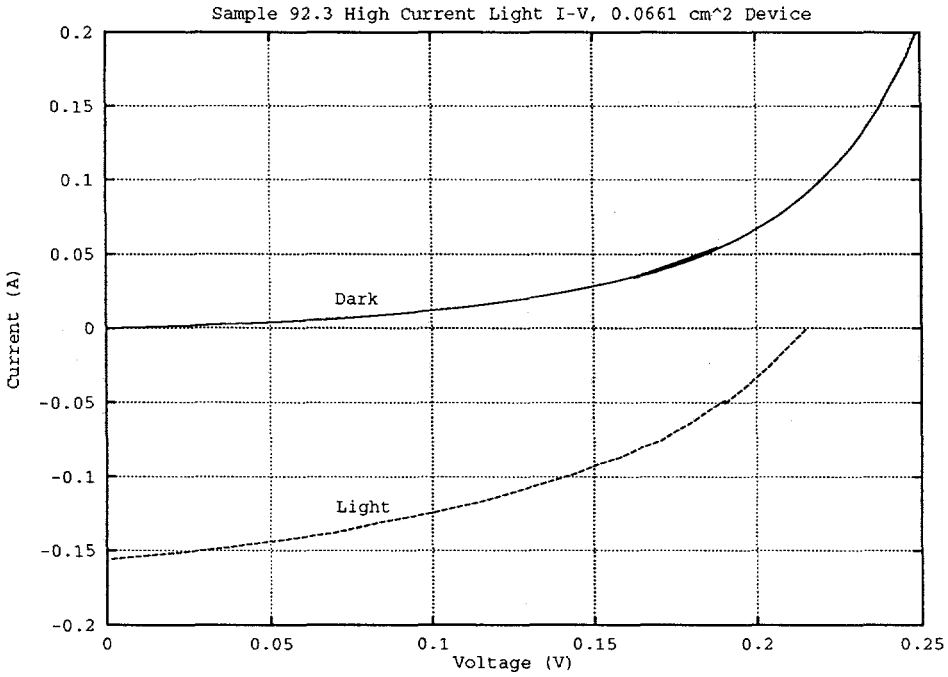

Figure 10: Generation 1 Ternary — Dark and Light I-V

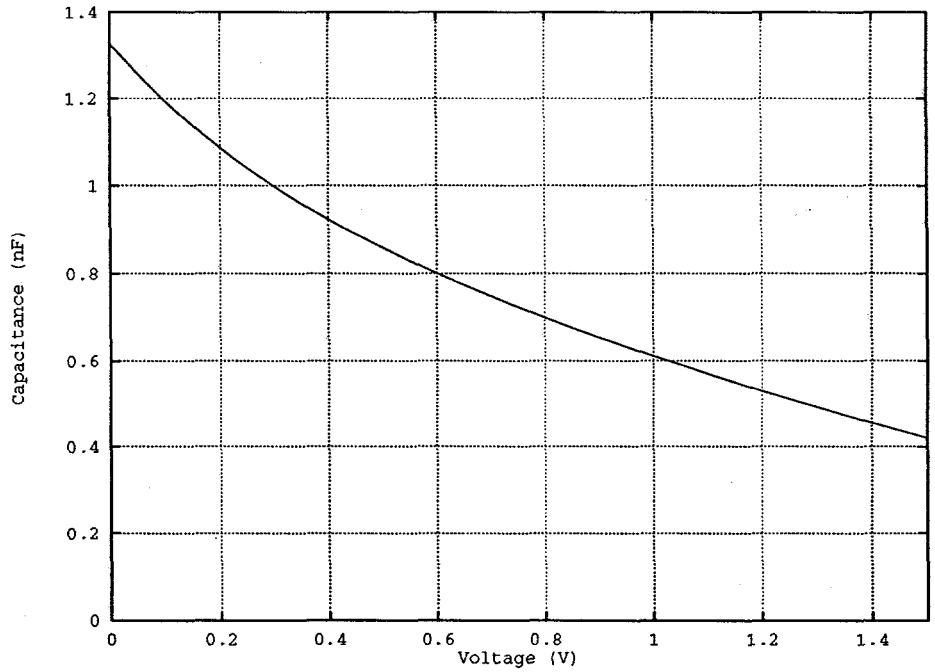

Figure 11: Generation 2 ternary — reverse bias C-V measurement taken at 10K

5 Summary and Conclusions

A series of working TPV test devices were formed from both ternary and quaternary epilayers on GaSb substrates. The devices exhibited properties consistent with the Schockley theory of semiconductor p-n junctions, exhibited photoresponse over the the wavelengths of interest, and generated electrical power when operated under field conditions. The photoresponse of the devices was poor at energies just above the bandgap, which is attributed to a short diffusion length in the n-type device base region (from one to two microns). The high intensity light I-V was not predicted accurately by a simple device model, which is attributed to either two-dimensional device effects, tunneling current, and/or a parasitic device nonlinearity.

References

[1] H. Ehsani, I. Bhat, C. Hitchcock, J. Borrego, and R. Gutmann. Characteristics of GaSb and GaInSb layers grown by metalorganic vapor phase epitaxy. *Proceedings of the Second NREL Conference on Thermophotovoltaic Generation of Electricity*, pages 423–433, 1995.

[2] H. Ehsani, I. Bhat, C. Hitchcock, and R. Gutmann. Growth and characterization of $In_{0.2}Ga_{0.8}Sb$ device structures using metalorganic vapor phase epitaxy. *Proceedings of the Third NREL Conference on Thermophotovoltaic Generation of Electricity*, 1997. to be published.

[3] J. G. Buglass, T. D. McLean, and D. G. Parker. A controllable etchant for fabrication of GaSb devices. *Journal of the Electrochemical Society: Solid-State Science and Technology*, 133(12):2565–2567, December 1986.

[4] J. McCaldin, T. McGill, and C. Mead. Schottky barriers on compound semiconductors: The role of the anion. *Journal of Vacuum Science and Technology*, 13(4):802–806, July/August 1976.

[5] M. Shur. *GaAs Device and Circuits.* Plenum Press, 1987.

[6] R. H. Cox and H. Strack. Ohmic contacts for GaAs devices. *Solid-State Electronics*, 10:1213–1218, 1967.

[7] G. P. Carver, J. J. Kopanski, D. B. Novotny, and R. A. Forman. Specific contact resistivity of metal-semiconductor contacts—a new, accurate method linked to spreading resistance. *IEEE Transactions on Electron Devices*, 35(4):489–496, April 1988.

[8] C. H. Heinz. Ohmic contacts to p- and n-type GaSb. *International Journal of Electronics*, 54(2):247–254, 1983.

[9] L. J. Gomez Zazo, M. T. Montojo, J. L. Castaño, and J. Piqueras. Chemical cleaning of GaSb (1,0,0) surfaces. *Journal of the Electrochemical Society*, 136(5):1480–1484, May 1989.

Appendix A Liftoff processing

A complex photoresist process was used to form the device front contacts in order to fabricate a thick contact with the poor step coverage required for liftoff. The photoresist processing steps are shown in table 3. Two layers of Hoescht-Celanese AZ4620 photoresist were deposited. The first layer was weakened by a flood UV exposure, and the second layer was added and exposed in the desired grid pattern. When the photoresist was developed, the exposed sections of the upper photoresist layer dissolved, allowing the developer to attack the lower layer photoresist and undercut the upper layer. A schematic of the photoresist structure after develop is shown in figure 12, with a micrograph of the actual photoresist structure shown in figure 13. When metal was evaporated onto this structure, the metal condensing on the sample surface was not connected to that on the photoresist, as shown in figure 14. Therefore, immersion in a photoresist solvent lifted off the unwanted metal successfully without damaging the contact metal.

1. Spin on AZ4620 at 7000 RPM for 40s.
2. Hot plate bake 15 minutes at 90°C.
3. Flood expose 1350mJ/cm^2.
4. Spin on AZ4620 at 7000 RPM 40s.
5. Hot plate bake 1 minute at 120°C.
6. Mask expose 450mJ/cm^2.
7. Develop in AZ401K 1 minute.

Table 3: Photoresist Processing

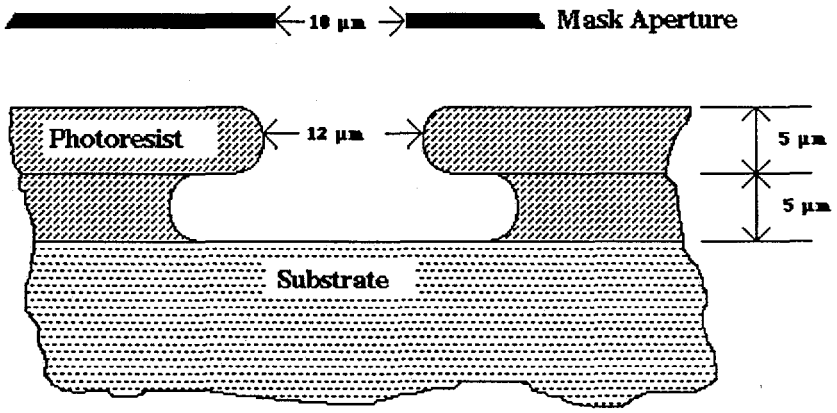

Figure 12: Photoresist Structure

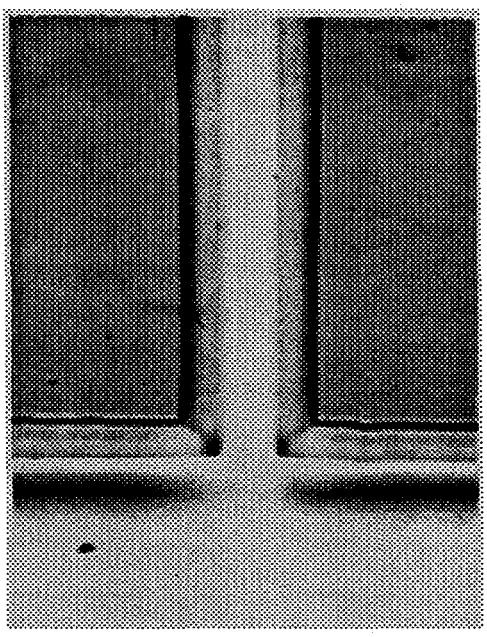

Figure 13: Thick Photoresist at the Intersection of a Grid Line and a Bus

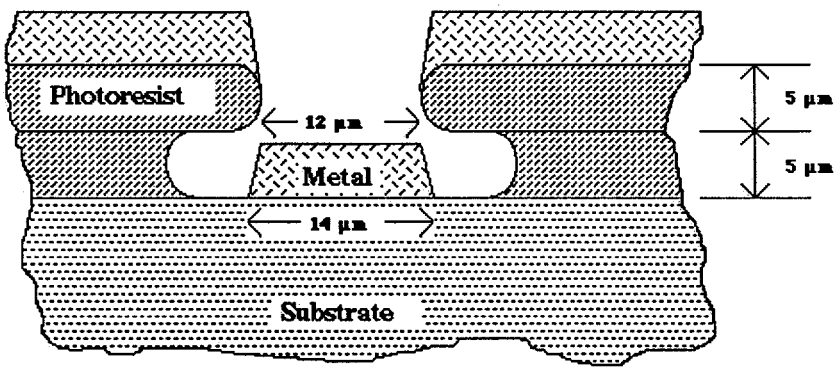

Figure 14: Structure after metal deposition